Journal of Computational and Applied Mathematics 342 (2018) 399–418

Contents lists available at ScienceDirect

Journal of Computational and Applied Mathematics

journal homepage: www.elsevier.com/locate/cam

A comparative study of limiting strategies in discontinuous Galerkin schemes for the M_1 model of radiation transport

Prince Chidyagwai [a], Martin Frank [b], Florian Schneider [c,*], Benjamin Seibold [d]

[a] Department of Mathematics and Statistics, Loyola University Maryland, 4501 N Charles Street, Baltimore, MD 21210, United States
[b] Department of Mathematics, RWTH Aachen University, Schinkelstr. 2, 52062 Aachen, Germany
[c] Fachbereich Mathematik, TU Kaiserslautern, Erwin-Schrödinger-Str., 67663 Kaiserslautern, Germany
[d] Department of Mathematics, Temple University, 1805 N Broad Street, Philadelphia, PA 19122, United States

ARTICLE INFO

Article history:
Received 30 June 2017
Received in revised form 27 February 2018

MSC:
35L40
65M08
65M60
65M70

Keywords:
Discontinuous Galerkin
Moment models
Minimum entropy
Realizability limiter

ABSTRACT

The M_1 minimum entropy moment system is a system of hyperbolic balance laws that approximates the radiation transport equation, and has many desirable properties. Among them are symmetric hyperbolicity, entropy decay, moment realizability, and correct behavior in the diffusion and free-streaming limits. However, numerical difficulties arise when approximating the solution of the M_1 model by high order numerical schemes; namely maintaining the realizability of the numerical solution and controlling spurious oscillations. In this paper, we extend a previously constructed one-dimensional realizability limiting strategy to 2D. In addition, we perform a numerical study of various combinations of the realizability limiter and the TVBM local slope limiter on a third order Discontinuous Galerkin (DG) scheme on both triangular and rectangular meshes. In several test cases, we demonstrate that in general, a combination of the realizability limiter and a TVBM limiter is necessary to obtain a robust and accurate numerical scheme. Our code is published so that all results can be reproduced by the reader.

1. Introduction

The M_1 model of radiative transfer is a nonlinear system of hyperbolic balance laws, and reads

$$\partial_t \psi^{(0)} + \nabla_x \cdot \psi^{(1)} = -\sigma_a \psi^{(0)} + q^{(0)} \tag{1.1a}$$

$$\partial_t \psi^{(1)} + \nabla_x \cdot \psi^{(2)}(\psi^{(0)}, \psi^{(1)}) = -(\sigma_s + \sigma_a)\psi^{(1)} + q^{(1)}, \tag{1.1b}$$

$$\psi^{(0)}(x, y, 0) = \psi_0^{(0)}(x, y), \qquad \psi^{(1)}(x, y, 0) = \psi_0^{(1)}(x, y). \tag{1.1c}$$

The quantities $\psi^{(0)}$, $\psi^{(1)}$, $\psi^{(2)}$ are, respectively, the zeroth (particle density), first (mean velocity) and second moment (pressure) over the unit sphere S^2 of the angular flux ψ,

$$\psi^{(0)} := \int_{S^2} \psi(\Omega) d\Omega, \quad \psi^{(1)} := \int_{S^2} \Omega \psi(\Omega) d\Omega, \quad \psi^{(2)} := \int_{S^2} \Omega \Omega^T \psi(\Omega) d\Omega,$$

* Corresponding author.
E-mail addresses: pchidyagwai@loyola.edu (P. Chidyagwai), frank@mathcces.rwth-aachen.de (M. Frank), schneider@mathematik.uni-kl.de (F. Schneider), seibold@temple.edu (B. Seibold).

https://doi.org/10.1016/j.cam.2018.04.017
0377-0427/

and are, respectively, a scalar, a vector, and a matrix. The system is supplemented by the closure condition

$$\psi^{(2)}(\psi^{(0)}, \psi^{(1)}) = D(\frac{\psi^{(1)}}{\psi^{(0)}})\psi^{(0)}, \tag{1.2}$$

where

$$D(n) = \frac{1-\chi(|n|)}{2}\mathrm{id} + \frac{3\chi(|n|)-1}{2}\frac{nn^T}{|n|^2} \text{ and } \chi(f) = \frac{3+4f^2}{5+2\sqrt{4-3f^2}} \text{ for } f \in [0,1]. \tag{1.3}$$

Here, D is a matrix, $n = \frac{\psi^{(1)}}{\psi^{(0)}}$ is a vector, and $f = |n|$ is a scalar. The quantity $\chi(f)$ is called the Eddington factor [1,2]. Let $X \subset \mathbb{R}^2$ be a bounded polygonal domain, then the system (1.1a)–(1.1b) can be written as a general first-order system of balance laws

$$\frac{\partial U}{\partial t} + \nabla \cdot \mathcal{F} = S, \text{ in } X \times (0,T) \tag{1.4}$$

$$U(x,y,0) = u_0(x,y), \text{ for } (x,y) \in X \tag{1.5}$$

where $\mathcal{F} = [F, G]$ and

$$U = \begin{bmatrix} \psi^{(0)} \\ \psi_x^{(1)} \\ \psi_y^{(1)} \end{bmatrix}, \; F = \begin{bmatrix} \psi_x^{(1)} \\ \psi_{xx}^{(2)} \\ \psi_{xy}^{(2)} \end{bmatrix}, \; G = \begin{bmatrix} \psi_y^{(1)} \\ \psi_{yx}^{(2)} \\ \psi_{yy}^{(2)} \end{bmatrix}, \; S = \begin{bmatrix} -\sigma_a\psi^{(0)} + q^{(0)} \\ -(\sigma_s+\sigma_a)\psi_x^{(1)} + q_x^{(1)} \\ -(\sigma_s+\sigma_a)\psi_y^{(1)} + q_y^{(1)} \end{bmatrix},$$

keeping in mind the closure relation (1.2). Here, $\psi_x^{(1)}$ and $\psi_y^{(1)}$ denote the first and second component of $\psi^{(1)}$, respectively, similarly for $\psi_{xx}^{(2)}$ to $\psi_{yy}^{(2)}$.

The system has to be complemented with boundary conditions of the form

$$U(x,y,t) = \gamma(x,y,t), \text{ for } (x,y) \in I(\partial X, U) \times (0,T), \tag{1.6}$$

where the operator I returns the influx boundaries, i.e. those parts of the boundary where information is transported into the domain [3]. Whether a part of the boundary is an influx boundary also depends on the solution itself, since the information direction can be read off the sign of the eigenvalues of the directional Jacobian in normal direction at these points. In our numerical experiments, we consider compactly supported initial data which do not reach the boundary before the final time. We prescribe Dirichlet boundary conditions identical to the initial conditions, hence the numerical solution is unaffected by the boundaries.

The expression for D in (1.3) comes from closing the moment system by an entropy closure using the entropy for photons. See for example [1,4–11] and references therein for more information. These references also discuss many properties which make the M_1 model, and entropy closures in general, quite appealing. Among these are symmetric hyperbolicity, i.e. the system can be transformed into a symmetric hyperbolic system, and a natural entropy–entropy flux pair, both of which ensure some level of well-posedness [3,12]. The hyperbolicity is of main interest in this work, and will be discussed in detail below. We especially focus on its connection to realizability — the fact that a moment vector can be reproduced by a non-negative particle density.

When the M_1 model is discretized using a monotone first-order scheme for hyperbolic equations (e.g. the Lax–Friedrichs scheme), it can be shown that the numerical solution will never leave the set of realizable moments [13]. This means that starting with a realizable initial condition, the numerical solution will be realizable at every time step. This is in particular required, since the model is not well-defined outside of the realizability set.

Unfortunately, and this is the main topic of this paper, higher-order numerical schemes do not automatically preserve this property, as will be discussed later. We use the Discontinuous Galerkin (DG) method, which provides a general framework to construct numerical schemes of arbitrary approximation order to solve hyperbolic balance laws. The original DG method was introduced in 1973 by Reed and Hill [14] for neutron transport and has been developed further to the Runge–Kutta Discontinuous Galerkin (RKDG) method by Cockburn et al. in a series of papers [15–19]. A $(k+1)$st order RKDG method uses a piecewise-polynomial approximation of degree k in space and a $(k+1)$st order strong stability preserving explicit Runge–Kutta scheme in time.

A DG scheme has to be supplemented by a limiting strategy. This typically consists of a slope limiter which ensures stability of the solution. A standard example of such a limiter is the TVBM (total variation bounded in the means) limiter [18]. For a system of balance laws, limiting the conserved variables component-wise can result in oscillations, due to the Gibbs phenomenon [20]. Instead, the limiter has to be applied in characteristic variables, i.e. Riemann invariants that are obtained by diagonalizing the system Jacobian [19,21]. In general, limiting in the characteristic variables gives superior results [13,22]. However, there are numerous examples for which the numerical solution obtained by limiting in the characteristic variables and component-wise limiting are comparable, e.g. [21,23–26]. In these situations, since the transformation to and from the characteristics requires additional computational effort, component-wise limiting is faster.

It has been shown in [13] that a robust numerical approximation of the M_1 model in 1D requires an additional limiter: a realizability limiter which ensures that the model remains well-posed. This has been extended to the general, one-dimensional, M_N case in [27]. In the current work, we extend this realizability limiting strategy to two dimensions. In addition, we demonstrate that in the absence of the realizability limiter, the TVBM limiter applied in the characteristic variables leads to a qualitatively superior solution compared to component-wise limiting; however, this limiter alone is not enough to guarantee moment realizability of the scheme.

The M_1 model therefore might serve as a good benchmark test for DG implementations, because it absolutely requires very careful limiting. We arrive at this conclusion experimentally, by running several well-known radiation transport test cases with two independently developed third-order DG schemes on unstructured triangular grids and regular rectangle grids.

The rest of this paper is organized as follows. In Section 2, we describe in detail the concept of realizability, and how it is connected to the well-posedness of the M_1 model. The DG implementations are described in Section 3. The realizability limiter will be developed and analyzed in Section 4. Section 5 contains the results from the test cases.

2. Properties of the M_1 model

From the general theory of moments one can deduce conditions on a given set of values, that are necessary and sufficient for the existence of a probability measure whose moments match these values [28]. Such moments are called realizable. In our case, we can restrict ourselves to measures that have a formal density (i.e. for the closure we allow Dirac δ's as densities). Given a scalar $\psi^{(0)}$ and a vector $\psi^{(1)}$, these are the zeroth and first moment of a non-negative density if and only if [28–30]

$$\psi^{(0)} > 0 \text{ and } |\psi^{(1)}| \leq \psi^{(0)}.$$

The interior of the realizable set is described by $\psi^{(0)} > 0$ and $|\psi^{(1)}| < \psi^{(0)}$. It has been shown in [31] that, under reasonable assumptions on the initial conditions, the analytical solution of the M_1 model in one spatial dimension remains realizable for all time. Until now, no similar statement could be made for the M_1 model in multiple dimensions or higher-order M_N models.

As mentioned before, the hyperbolicity of the M_1 model is a direct consequence of the entropy closure. Additional insight can be obtained by computing the eigenvalues explicitly. Given a unit direction vector $\boldsymbol{n} = (n_x, n_y)^T$, we have to determine the eigenvalues of the directional Jacobian

$$n_x J_x(U) + n_y J_y(U), \tag{2.1}$$

where J_x and J_y are the Jacobians of F and G, respectively. Because of the invariance of the model under coordinate transformations, the eigenvalues can only depend on the angle between $\psi^{(1)}$ and $\boldsymbol{n}$, and the absolute value $\frac{|\psi^{(1)}|}{\psi^{(0)}}$. The eigenvalues can be computed analytically, but the formulas are very lengthy so we do not show them here (cf. [32]). Fig. 1 shows the eigenvalues for two different angles. The most important observation is that the eigenvalues collapse into one value at the boundary of the realizability region, i.e. for $\frac{|\psi^{(1)}|}{\psi^{(0)}} = 1$. Inspection of the Jacobian shows that at that boundary the Jacobian is no longer diagonalizable, i.e. the M_1 model loses (strict) hyperbolicity. This means that the M_1 model is only well-posed in the interior of the domain of realizability. As a consequence, in a numerical scheme one should always ensure staying in the interior of the realizability domain.

3. Runge–Kutta discontinuous Galerkin method

3.1. Spatial discretization

In this section, we describe the Runge–Kutta Discontinuous Galerkin method (RKDG) for solving (1.4)–(1.6). Following the approach outlined in a series of papers by Cockburn and Shu [15–17,19], we discretize in space using piece-wise polynomials of degree k, that are allowed to be discontinuous at the cell interface. The time discretization is performed by a strong stability preserving explicit Runge–Kutta scheme of order $k+1$ [33].

In the following, let $\mathcal{T}_h$ be a partition of a polygonal computational domain X and K be an element in $\mathcal{T}_h$ with boundary edges e. For each $t \in [0, T]$, we seek an approximate solution $U_h(x, t)$ in the DG space

$$V_h^k = \{v \in L^\infty(X) : v|_K \in P^k(K), \forall K \in \mathcal{T}_h\}$$

where $P^k(K)$ is the set of polynomials of degree k. We follow the Galerkin approach: first we multiply (1.4) by a smooth test function v and integrate by parts over each element. We replace the exact solution U and smooth test function v by the approximation solution U_h and v_h (both in V_h^k) respectively to obtain:

$$\begin{aligned} &\frac{d}{dt}\int_K U_h(x,t)v_h(x)\,dx + \sum_{e\in\partial K}\int_e \mathcal{F}(U_h(x,t))\cdot \boldsymbol{n}_{e,K}\, v_h(x)\,d\Gamma \\ &- \int_K \mathcal{F}(U_h(x,t))\cdot\nabla v_h(x)\,dx = \int_K S\big(U_h(x,t)\big)v_h(x)\,dx \quad \forall v_h \in V_h^k, \end{aligned} \tag{3.1}$$

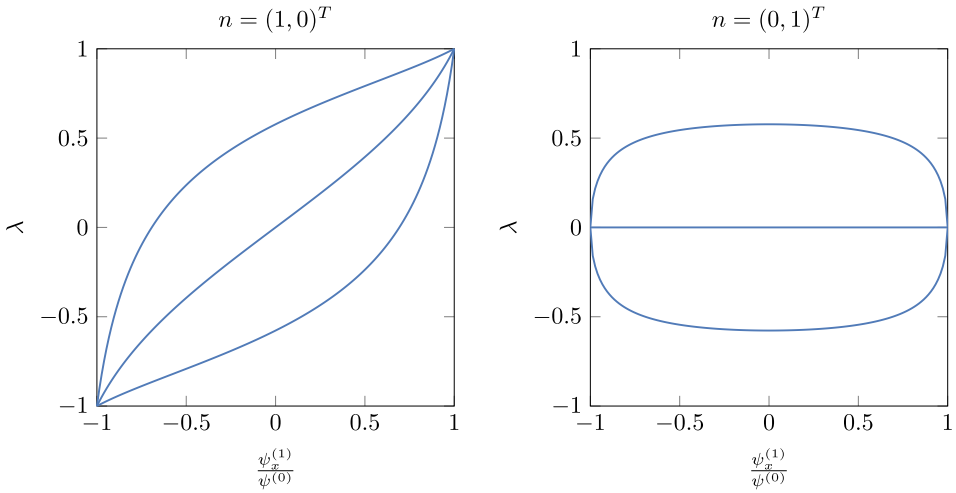

Fig. 1. Eigenvalues of the M_1 model as a function of $\frac{\psi_x^{(1)}}{\psi^{(0)}}$ for $\psi_y^{(1)} = 0$ and two values of n.

where $\boldsymbol{n}_{e,K}$ is the outward unit normal to the boundary of K. We take $U_h(x, 0)$ on each element to be the L_2-projection of the initial condition on V_h^k, i.e.,

$$\int_K U_h(x, 0)v_h(x)\,dx = \int_K u_0 v_h(x)\,dx, \quad \forall v_h \in V_h^k. \tag{3.2}$$

The choice of a discontinuous basis implies that our approximate solution $U_h(x, t)$ is discontinuous across edges. In this case the normal trace $\mathcal{F}(U_h(x, t)) \cdot \boldsymbol{n}_{e,K}$ is not defined on the element boundary ∂K. We replace the normal trace by a numerical flux function $H_{e,K}(x, t)$ that depends on the approximate solution from the interior and exterior of the element K. Thus we define

$$H_{e,K}(x, t) = H_{e,K}(U_h(x^{int\{K\}}, t), U_h(x^{ext\{K\}}, t)), \tag{3.3}$$

where

$$U_h(x^{int\{K\}}, t) = \lim_{\xi \to (x,y) \in K} U_h(\xi, t),$$

for the approximate solution defined from the interior of the element K and

$$U_h(x^{ext\{K\}}, t) = \begin{cases} \gamma_h(x, t) & \text{if } x \in \partial X, \\ \lim\limits_{\xi \to (x,y) \notin K} U_h(\xi, t), & \text{otherwise} \end{cases}$$

for the points on the exterior of K. Using the numerical flux (3.3), the discrete weak formulation (3.1)–(3.2) becomes

$$\begin{aligned} &\frac{d}{dt}\int_K U_h(t, x)v_h(x)\,dx + \sum_{e \in \partial K} \int_e H_{e,K}(U_h(x^{int\{K\}}, t), U_h(x^{ext\{K\}}, t))v_h(x)\,d\Gamma \\ &- \int_K \mathcal{F}(U_h(x, t)) \cdot \nabla v_h(x)\,dx = \int_K S(U_h(t, x))v_h(x)\,dx, \quad \forall v_h \in V_h^k, \end{aligned} \tag{3.4}$$

$$\int_K U_h(x, 0)v_h(x)\,dx = \int_K u_0 v_h(x)\,dx, \quad \forall v_h \in V_h^k. \tag{3.5}$$

We choose the global Lax–Friedrichs flux

$$H_{e,K}(a, b) = \frac{1}{2}\Big[\mathcal{F}(a) \cdot \boldsymbol{n}_{e,K} + \mathcal{F}(b) \cdot \boldsymbol{n}_{e,K} - \alpha(b - a)\Big], \tag{3.6}$$

where the numerical viscosity constant α is taken as the global estimate of the absolute value of the largest eigenvalue of the Jacobian (2.1). For the M_1 model, we can take $\alpha = 1$.

Boundary conditions (1.6) have to be incorporated via the quantities $U_h(x^{ext\{K\}}, t)$ in the edge integral, if the edge e is part of the boundary. We take the simplest approach possible by adding so-called "ghost cells" which are then filled with the corresponding values for U. Note, however, that the validity of this approach, due to its inconsistency with the original boundary conditions (1.6), is not entirely non-controversial, but the question of appropriate boundary conditions for moment models is an open problem [34–38] which is not explored here.

Eqs. (3.4)–(3.5) can be written as a system of ODEs on each element after inverting the mass matrix in (3.4). Indeed, let $\{\varphi_1, \varphi_2, \ldots, \varphi_{N_k}\}$ denote a basis of the space of polynomials of degree k on cell K, where $N_k = \frac{1}{2}(k+1)(k+2)$. On each element, the DG approximate solution U_h of the components has the form

$$\psi^{(0)} = \sum_{i=1}^{N_k} \alpha_i^{\psi^{(0)}} \varphi_i, \quad \psi_x^{(1)} = \sum_{i=1}^{N_k} \alpha_i^{\psi_x^{(1)}} \varphi_i, \text{ and } \psi_y^{(1)} = \sum_{i=1}^{N_k} \alpha_i^{\psi_y^{(1)}} \varphi_i, \tag{3.7}$$

where $\alpha_i^{\psi^{(0)}}, \alpha_x^{\psi^{(1)}}, \alpha_y^{\psi^{(1)}}$ are unknowns to be determined. Using the form of the approximate solution in (3.7), we can write (3.4)–(3.5) in matrix form:

$$\boldsymbol{M}\frac{\partial}{\partial t}\alpha_h + \boldsymbol{H}\alpha_h - \boldsymbol{F}\alpha_h = \boldsymbol{S}\alpha_h \tag{3.8}$$

$$\boldsymbol{M}\alpha_h^0 = \boldsymbol{U}_0 \tag{3.9}$$

where α_h is the vector of solution coefficients and

$$(\boldsymbol{M})_{ij} = \int_K \varphi_j\varphi_i, \quad (\boldsymbol{H})_i = \sum_{e\in\partial K}\int_e H_{e,K}(x,t)\varphi_i, \quad (\boldsymbol{F})_i = \int_K \mathcal{F}(U_h)\cdot\nabla\varphi_i \tag{3.10}$$

$$(\boldsymbol{S})_i = \int_K S(U_h)\varphi_i, \text{ and } (\boldsymbol{U}_0)_i = \int_K u_0\varphi_i. \tag{3.11}$$

The complete coefficient vector is given by $\alpha_h = \{\alpha_1^{\psi^{(0)}}, \ldots, \alpha_{N_k}^{\psi^{(0)}}, \alpha_1^{\psi_x^{(1)}}, \ldots, \alpha_{N_k}^{\psi_x^{(1)}}, \alpha_1^{\psi_y^{(1)}}, \ldots, \alpha_{N_k}^{\psi_y^{(1)}}\}$, where $\alpha_i^{\psi^{(0)}}, \alpha_i^{\psi_x^{(1)}}, \alpha_i^{\psi_y^{(1)}}$ are the coefficients of the numerical approximation to the zeroth and first order moments, respectively. We can write (3.8)–(3.9) in the form

$$\frac{d}{dt}\alpha_h = \mathcal{L}_h(\alpha_h), \quad \text{on } X\times(0,T) \tag{3.12}$$

$$\alpha_h(x,0) = \alpha_h^0 \tag{3.13}$$

where

$$\mathcal{L}_h(\alpha_h) = \boldsymbol{M}^{-1}(\boldsymbol{S}\alpha_h + \boldsymbol{F}\alpha_h - \boldsymbol{H}\alpha_h). \tag{3.14}$$

We approximate the solution by discontinuous quadratic polynomials in space and the third-order strong stability preserving Runge–Kutta time discretization scheme proposed in [39,40], also known as the Shu–Osher scheme. Let $\{t^n\}_{n=0}^N$ be a partition of $[0,T]$ and let $\Delta t = t^{n+1} - t^n$, $n = 0, \ldots, N-1$, then the time stepping scheme updating the coefficients of the DG polynomials can be written as:

- Set $\alpha^0 = \boldsymbol{M}^{-1}\boldsymbol{U}_0$;
- For $n = 1, \ldots, N-1$ compute α_h^{n+1} as follows:
  1. $\alpha_h^{(1)} = \alpha_h^n + \Delta t_n \mathcal{L}_h(\alpha_h^n)$
  2. $\alpha_h^{(2)} = \frac{3}{4}\alpha_h^n + \frac{1}{4}(\alpha_h^{(1)} + \Delta t_n \mathcal{L}_h(\alpha_h^{(1)}))$
  3. $\alpha_h^{(3)} = \frac{1}{3}\alpha_h^n + \frac{2}{3}(\alpha_h^{(2)} + \Delta t_n \mathcal{L}_h(\alpha_h^{(2)}))$
  4. Set $\alpha_h^{n+1} = \alpha_h^{(3)}$.

This Runge–Kutta method is a convex combination of (iterated) forward Euler steps. Using the convexity of the realizability domain, one can show that it preserves realizability under a specific CFL-condition. We use this property to achieve high order also in time without the need of dealing with complicated time-discretizations in the proof of realizability preservation.

3.2. Quadrature rules

The assembly of the discrete operator $\mathcal{L}_h(\alpha_h)$ (3.12) is done using numerical quadrature that is exact for polynomials of degree $2k+1$ for edge integrals, and degree $2k$ for volume integrals, respectively for both the rectangular and triangular meshes. In addition, we will need a modified Gaussian quadrature rule to construct the realizability limiter. This rule consists of quadrature points in the interior of the cell and on its boundary where the latter form one-dimensional quadratures on the element edges. This is crucial to balance the different appearing types of spatial integrals in the proof of the realizability-preserving property. These rules are described in the following section that closely follows the construction in [41].

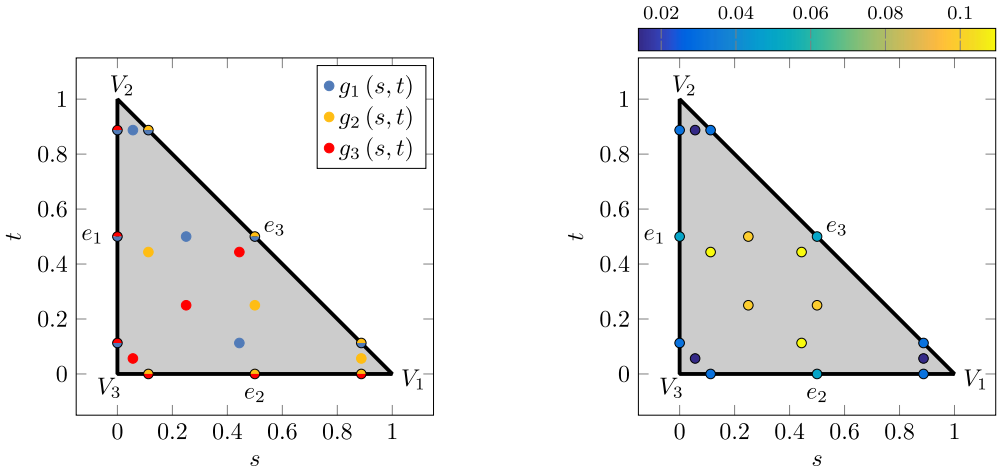

(a) Positions. (b) Weights.

Fig. 2. Position of the quadrature nodes under the three projections g_i. The color corresponds to the weight $\tilde{w}^\gamma$ at the quadrature node.

3.2.1. Triangles

We start with two quadrature rules on the interval $[-\frac{1}{2}, \frac{1}{2}]$, a Gaussian rule

$$v^\beta = \frac{1}{2}\left(-\sqrt{\frac{3}{5}} \quad 0 \quad \sqrt{\frac{3}{5}}\right), \quad w^\beta = \frac{1}{18}\begin{pmatrix}5 & 8 & 5\end{pmatrix}$$

and a Gauss–Lobatto rule

$$u^\alpha = \frac{1}{2}\begin{pmatrix}-1 & 0 & 1\end{pmatrix}, \quad \hat{w}^\alpha = \frac{1}{6}\begin{pmatrix}1 & 4 & 1\end{pmatrix}. \tag{3.15}$$

We map the tensor product rule of those Gauss and Gauss–Lobatto quadrature rules from the square $[-\frac{1}{2}, \frac{1}{2}]^2$ onto the triangle K with vertices $V_1^K, \ldots, V_3^K$ using the three degenerate projections

$$\begin{aligned}
g_1(u,v) &= (\tfrac{1}{2}+v)V_1^K + (\tfrac{1}{2}+u)(\tfrac{1}{2}-v)V_2^K + (\tfrac{1}{2}-u)(\tfrac{1}{2}-v)V_3^K \\
g_2(u,v) &= (\tfrac{1}{2}+v)V_2^K + (\tfrac{1}{2}+u)(\tfrac{1}{2}-v)V_3^K + (\tfrac{1}{2}-u)(\tfrac{1}{2}-v)V_1^K \\
g_3(u,v) &= (\tfrac{1}{2}+v)V_3^K + (\tfrac{1}{2}+u)(\tfrac{1}{2}-v)V_1^K + (\tfrac{1}{2}-u)(\tfrac{1}{2}-v)V_2^K.
\end{aligned}$$

Let $\bar{U}_K$ denote the cell average of the numerical solution U_h represented by the DG polynomial p_K on triangle K, following [41] it holds that

$$\bar{U}_K = \frac{2}{3}\sum_{i=1}^{3}\sum_{\alpha=1}^{3}\sum_{\beta=1}^{3} p_K\left(g_i\left(\hat{u}^\alpha, v^\beta\right)\right)\left(\frac{1}{2}-v^\beta\right) w^\alpha \hat{w}^\beta.$$

Note that the Gauss–Lobatto points on the edge are always taken twice (see Fig. 2).

The authors of [41] showed that the cell mean can be constructed as the following convex combination of inner and boundary points:

$$\bar{U}_K = \sum_{i=1}^{3}\frac{2}{3} w^\beta \hat{w}^{\alpha=1} U_{i,\beta}^{int} + \sum_{\gamma=1}^{L} \tilde{w}^\gamma U_\gamma^{inner} \tag{3.16}$$

where U_γ^{inner} and $U_{i,\beta}^{int}$ represent the evaluation of the DG polynomial p_K at the respective interior and boundary quadrature nodes $(x_\gamma^{inner}, y_\gamma^{inner})$ and $(x_{i,\beta}^{int}, y_{i,\beta}^{int})$ (compare Fig. 2), and $L = 3(N-2)(k+1) = 9$ is the number of inner points. With this we obtain a quadrature rule with 18 points which is accurate for polynomials of order $2k-1 = 3$.

The flux term in (3.4) should be approximated by the $1D$ $(k+1)$ point Gauss quadrature with weights w^β:

$$\sum_{e\in\partial K}\int_e H_{e,K}(x,t)\varphi_i^K(x)\,d\Gamma = \sum_{i=1}^{3}\sum_{\beta=1}^{3} H_{e_i,K}(U_{i,\beta}^{int}, U_{i,\beta}^{ext}, t)\varphi_i^K(x_{i,\beta}^{int}, y_{i,\beta}^{int}) w^\beta l_K^i \tag{3.17}$$

where l_K^i is the length of edge e_i^K.

3.2.2. Rectangles

For the assembly of the discrete operator in the rectangular DG code we use a tensor quadrature rule of the 1D 4-point Gauss–Lobatto rule on $[-\frac{1}{2}, \frac{1}{2}]$:

$$u^{\alpha} = \frac{1}{2\sqrt{5}}\begin{pmatrix} -\sqrt{5} & -1 & 1 & \sqrt{5} \end{pmatrix}, \quad \hat{w}^{\alpha} = \frac{1}{12}\begin{pmatrix} 1 & 5 & 5 & 1 \end{pmatrix}.$$

However for the proof of our main theorem we only need the three point rule (3.15) which will give a weaker CFL-condition.

3.3. Slope limiting

In order to enforce stability [42,43] and to mitigate numerical oscillations caused by the Gibbs phenomenon we apply a slope limiter to every stage of the Runge–Kutta time stepping scheme. We implement the slope limiter detailed by Cockburn and Shu in [15]

$$\overline{m}(a_1, a_2, \ldots, a_n) = \begin{cases} a_1 & \text{if } |a_1| < M(\Delta x)^2 \\ m(a_1, a_2, \ldots, a_n) & \text{otherwise,} \end{cases} \tag{3.18}$$

where M is an estimated bound on the second derivative of the solution around smooth extrema [16], Δx is the characteristic length of each element and m is the minmod function

$$m(a_1, a_2, \ldots, a_n) = \begin{cases} \operatorname{sign}(a_1)\min\{|a_1|, |a_2|, \ldots, |a_n|\} & \text{if } \operatorname{sign}(a_1) = \operatorname{sign}(a_2) = \cdots = \operatorname{sign}(a_n), \\ 0 & \text{else.} \end{cases}$$

The limiter can be applied component-wise to the primitive variables or in the characteristic variables. For limiting in the characteristic variables we first construct a matrix $\mathcal{R}$ that diagonalizes the directional Jacobian in the normal direction $\boldsymbol{n} = (n_x, n_y)$ evaluated at the mean in each element

$$\mathcal{R}^{-1}(n_x J_x(\overline{U}_k) + n_y J_y(\overline{U}_k))\mathcal{R} = \Lambda. \tag{3.19}$$

Applying the limiter in the characteristic variables ensures that the solution is total variation bounded in the means (TVBM).

4. Realizability limiter

We want to construct a scheme so that the numerical solution stays realizable with respect to the cell means. The proofs presented in this section follow the strategy used in [44], which has also been used in the construction of realizability-preserving limiters for the M_1 model in 1D [13].

First we need a technical lemma.

Lemma 4.1. *Let $\nu \in \mathbb{R}^2$ be an arbitrary unit vector. For the M_1 model the combination of moments $(\psi^{(0)} \pm \psi^{(1)} \cdot \nu, \psi^{(1)} \pm \psi^{(2)} \cdot \nu)$ is realizable.*

Proof. Let ψ be a non-negative density that realizes $\psi^{(0)}$ and $\psi^{(1)}$. Then $(1 \pm \nu \cdot \Omega)\psi(\Omega)$ is a non-negative density that realizes the combined moments. □

Let us now consider the higher-order scheme (3.4). Due to the convexity of the realizable set it suffices to investigate the forward-Euler discretization in time since the used SSP integrator is just a convex combination of such Euler steps.

Theorem 4.2 (*Main Result*)**.** *One forward-Euler step of the scheme (3.4) with the DG polynomial p_K of degree k yields realizable cell averages if $p_K(x_s, y_s)$ is realizable for all $(x_s, y_s) \in S_k^K$ and if the CFL condition*

$$\frac{2}{3}\hat{w}_1\left(1 - \Delta t\,(\sigma_a + \sigma_s)\right) - \frac{\Delta t}{2\,|K|} l_K^i \geq 0 \;\; \forall i = 1, \ldots, 3 \tag{4.1}$$

holds. Here $\hat{w}_1$ is the quadrature weight of the N-point Gauss–Lobatto rule on $[-\frac{1}{2}, \frac{1}{2}]$ for the first quadrature point.

Proof. For simplicity assume that $\sigma_s = \sigma_a = 0$ and $q = 0$. Furthermore, to ease notation, we drop the symbol n for all quantities at the current time step. After application of the forward-Euler scheme the cell averages in element K satisfy

$$\begin{aligned} \overline{U}_K^{n+1} &= \overline{U}_K - \frac{\Delta t}{|K|}\sum_{i=1}^{3}\int_{e_i} H_{e_i,K}\left(U_K^{int}, U_{K(i)}^{ext}\right) dx \\ &\overset{(3.6)}{=} \begin{pmatrix} \bar{\psi}_K^{(0)} \\ \bar{\psi}_K^{(1)} \end{pmatrix} - \frac{\Delta t}{2\,|K|}\sum_{i=1}^{3}\int_{e_i}\begin{pmatrix} \psi_K^{(0)} \\ \psi_K^{(1)} \end{pmatrix} dx + \frac{\Delta t}{2\,|K|}\sum_{i=1}^{3}\int_{e_i}\begin{pmatrix} \psi_{K(i)}^{(0)} - \psi_{K(i)}^{(1)} \cdot \boldsymbol{n}_{e_i,K} \\ \psi_{K(i)}^{(1)} - \psi_{K(i)}^{(2)} \cdot \boldsymbol{n}_{e_i,K} \end{pmatrix} dx, \end{aligned}$$

where $U_K = p_K$ and $U_{K(i)} = p_{K(i)}$ denote the polynomial representations of U_h on element K and on its neighbor $K(i)$ sharing edge e_i with K, respectively.

Evaluating the second integral using the Gaussian quadrature as in (3.17) it is easy to see by using Lemma 4.1 that on each edge e_i the quantity

$$\int_{e_i} \begin{pmatrix} \psi^{(0)}_{K(i)} - \psi^{(1)}_{K(i)} \cdot \boldsymbol{n}_{e_i,K} \\ \psi^{(1)}_{K(i)} - \psi^{(2)}_{K(i)} \cdot \boldsymbol{n}_{e_i,K} \end{pmatrix} dx = l^i_K \sum_{\beta=1}^{k+1} w^\beta \begin{pmatrix} \psi^{(0)}_{K(i),\beta} - \psi^{(1)}_{K(i),\beta} \cdot \boldsymbol{n}_{e_i,K} \\ \psi^{(1)}_{K(i),\beta} - \psi^{(2)}_{K(i),\beta} \cdot \boldsymbol{n}_{e_i,K} \end{pmatrix}$$

is realizable since $\sum w^\beta = 1$. Here, $\psi^{(0)}_{K(i),\beta}$ denotes the evaluation of the polynomial representation of $\psi^{(0)}$ on the neighboring element $K(i)$ at the quadrature node associated with w^β on e_i and similarly for all other moments.

Now it suffices to show that the first terms in this equation are realizable, too. We rewrite the cell average into a combination of interior points and edge points:

$$\overline{U}_K \overset{(3.16)}{=} \sum_{i=1}^{3} \sum_{\beta=1}^{k+1} \frac{2}{3} w^\beta \hat{w}^1 U^{int}_{i,\beta} + \sum_{\gamma=1}^{L} \tilde{w}^\gamma U^{inner}_\gamma,$$

$$\int_{e_i} U_K \, dx = \sum_{\beta=1}^{k+1} w^\beta l^i_K U^{int}_{i,\beta}.$$

Then

$$\begin{pmatrix} \bar{\psi}^{(0)}_K \\ \bar{\psi}^{(1)}_K \end{pmatrix} - \frac{\Delta t}{2\,|K|} \sum_{i=1}^{3} \int_{e_i} \begin{pmatrix} \psi^{(0)}_K \\ \psi^{(1)}_K \end{pmatrix} dx = \sum_{\gamma=1}^{L} \tilde{w}^\gamma U^{inner}_\gamma + \sum_{i=1}^{3} \sum_{\beta=1}^{k+1} w^\beta U^{int}_{i,\beta} \left(\frac{2}{3} \hat{w}^1 - \frac{\Delta t}{2\,|K|} l^i_K \right).$$

Under the CFL condition, we immediately get that

$$\sum_{\gamma=1}^{L} \tilde{w}^\gamma U^{inner}_\gamma + \sum_{i=1}^{3} \sum_{\beta=1}^{k+1} w^\beta U^{int}_{i,\beta} \left(\frac{2}{3} \hat{w}^1 - \frac{\Delta t}{2\,|K|} l^i_K \right)$$

is realizable since the quadrature weights sum up to 1.

For absorption and scattering we assume for simplicity that σ_s and σ_a are constant in K. Then we can write the cell averages of the source term as

$$\begin{aligned} \overline{S(U_K)} = &\sum_{i=1}^{3} \sum_{\beta=1}^{k+1} \frac{2}{3} w^\beta \hat{w}^1 \left(\sigma_a U^{int}_{i,\beta} + \sigma_s \begin{pmatrix} 0 \\ \psi^{(1)}_{i,\beta,int} \end{pmatrix} \right) \\ &+ \sum_{\gamma=1}^{L} \tilde{w}^\gamma \left(\sigma_a U^{inner}_\gamma + \sigma_s \begin{pmatrix} 0 \\ \psi^{(1)}_{\gamma,inner} \end{pmatrix} \right). \end{aligned}$$

Thus the updated cell averages can be written as the moments of a non-negative distribution, i.e. $U^{n+1}_K = \int \begin{pmatrix} 1 \\ \Omega \end{pmatrix} \Xi_K(\Omega)\, d\Omega$ with

$$\begin{aligned} \Xi_K = &\sum_{\gamma=1}^{L} \tilde{w}^\gamma \left[(1 - \Delta t\,(\sigma_a + \sigma_s))\, \psi^{inner}_\gamma + \frac{\sigma_s}{4\pi} \int \psi^{inner}_\gamma \, d\Omega \right] \\ &+ \sum_{i=1}^{3} \sum_{\beta=1}^{k+1} w^\beta \left[\psi^{int}_{i,\beta} \left(\frac{2}{3} \hat{w}^1 (1 - \Delta t\,(\sigma_a + \sigma_s)) - \frac{\Delta t}{2\,|K|} l^i_K \right) + \frac{\Delta t}{2\,|K|} l^i_K \psi_{K(i),\beta} + \frac{\sigma_s}{4\pi} \int \psi^{int}_{i,\beta} \, d\Omega \right]. \end{aligned}$$

The quantity ψ^{inner}_γ is any nonnegative distribution function realizing U^{inner}_γ, similarly for $\psi^{int}_{i,\beta}$ and $\psi_{K(i),\beta}$. It is easy to see that under the given assumptions $\Xi^n_K \geq 0$, which implies that U^{n+1}_K is by definition realizable. □

A similar result can be obtained on the rectangular grid by going through the same lines of the previous proof, replacing the quadrature rules on the triangle with those on the rectangles. More details can be found in [29].

Theorem 4.3 (*Main Result for Rectangular Grid*). *One forward-Euler step of the scheme (3.4) with the DG polynomial p_K of degree k yields realizable cell averages if $p_K(x_s, y_s)$ is realizable for all $(x_s, y_s) \in S^K_k$ and if the CFL condition*

$$\hat{w}_1 (1 - \Delta t\,(\sigma_a + \sigma_s)) - \frac{\Delta t}{\Delta x} - \frac{\Delta t}{\Delta y} \geq 0 \tag{4.2}$$

holds. Here $\hat{w}_1$ is the quadrature weight of the N-point Gauss–Lobatto rule on $[-\frac{1}{2}, \frac{1}{2}]$ for the first quadrature point.

Remark 4.4. We want to note that the required CFL conditions (4.1) and (4.2) are not any more restrictive than what standard DG methods generally incur. Assume for simplicity $\sigma_a = \sigma_s = 0$ and consider (4.2), the stability condition for the DG scheme reads

$$\frac{\Delta t}{\Delta x} + \frac{\Delta t}{\Delta y} \leq \frac{1}{2k+1}, \tag{4.3}$$

where k denotes the polynomial degree used. We collect the corresponding values for the classical and our modified CFL condition in the following table, where $\hat{w}_1$ is taken from the N-point Gauß–Lobatto rule that integrates polynomials of degree k:

k	0	1	2	3	4
$\frac{1}{2k+1}$	1	$\frac{1}{3}$	$\frac{1}{5}$	$\frac{1}{7}$	$\frac{1}{9}$
$\hat{w}_1$	1	$\frac{1}{2}$	$\frac{1}{6}$	$\frac{1}{6}$	$\frac{1}{12}$

Note that $\hat{w}_1 = \frac{1}{4}k^2 + k + \frac{3}{4}$ for k odd. It can be seen that these values are in a similar range for reasonably small k.

All that remains is to ensure that the assumptions of the two theorems are satisfied. This can be achieved by a simple scaling limiter. A similar limiter has been derived in other contexts, e.g. shallow water [45], Euler equations [44] and gas dynamics [46]. The basic idea is to dampen the higher-order parts of the DG polynomial $p_K(x, y)$ until at all quadrature nodes $(x_s, y_s) \in S_k^K$ the evaluation $p_K(x_s, y_s)$ is realizable. It has been reported in [46] that this limiter, due to its simplicity, can destroy the formal accuracy of the scheme in certain non-generic situations. This has been investigated in a one-dimensional setting for minimum-entropy models in [27]. There, it has been shown that close to the realizability boundary the convergence order can drop. However, we still expect order preservation in most practical cases.

Writing the limited polynomial as

$$p_K^\theta(x, y) := \theta\overline{p_K} + (1-\theta)p_K(x, y) \overset{(3.7)}{=} \theta\alpha_1^U\varphi_1 + (1-\theta)\sum_{i=1}^{N_k}\alpha_i^U\varphi_i = \alpha_1^U\varphi_1 + (1-\theta)\sum_{i=2}^{N_k}\alpha_i^U\varphi_i$$

it becomes clear that the cell average of p_K is preserved and only higher-order coefficients are damped by the factor $(1-\theta)$ where θ is chosen as the minimal value in the set

$$\left\{\tilde{\theta} \in [0, 1] \mid p_K^{\tilde{\theta}}(x_s, y_s) \text{ is realizable for all } (x_s, y_s) \in S_k^K\right\}. \tag{4.4}$$

Such a θ always exist under the assumption that $\overline{p_K}$ is realizable as a consequence of the convexity of the realizable set. To calculate θ_s it suffices to find the intersections of the ray segments

$$\left\{\theta\bar{U}_K + (1-\theta)p_K(x_s, y_s) \mid \theta \in [0, 1]\right\},\ (x_s, y_s) \in S_k^K \tag{4.5}$$

with the boundary of the realizable set

$$\left\{\left(\psi^{(0)}, \psi^{(1)}\right) \in \mathbb{R}^3 \mid \psi^{(0)} = \left|\psi^{(1)}\right|\right\} = \left\{\left(\psi^{(0)}, \psi^{(1)}\right) \in \mathbb{R}^3 \mid \psi^{(0)} \geq 0,\ \left(\psi^{(0)}\right)^2 = \left|\psi^{(1)}\right|^2\right\}. \tag{4.6}$$

Using the condition $\left(\psi^{(0)}\right)^2 = \left|\psi^{(1)}\right|^2$ from (4.6) and the parameterization of the ray segment (4.5) we get

$$\left(\theta\bar{\psi}^{(0)} + (1-\theta)\psi^{(0)}\right)^2 \overset{!}{=} \left(\theta\bar{\psi}_y^{(1)} + (1-\theta)\psi^{(1)}\right)^2 + \left(\theta\bar{\psi}_y^{(1)} + (1-\theta)\psi^{(1)}\right)^2.$$

Rearranging this expression, collecting the coefficients in powers of θ yields the polynomial equation

$$\begin{aligned}
0 \overset{!}{=} r(\theta) &= a\theta^2 + b\theta + c,\\
a &= -\left(\bar{\psi}^{(0)} - \psi^{(0)}\right)^2 + \left(\bar{\psi}_x^{(1)} - \psi_x^{(1)}\right)^2 + \left(\bar{\psi}_y^{(1)} - \psi_y^{(1)}\right)^2\\
b &= 2\cdot\left(\left(\psi^{(0)}\right)^2 - \bar{\psi}^{(0)}\cdot\psi^{(0)} - \left(\psi_x^{(1)}\right)^2 + \bar{\psi}_x^{(1)}\cdot\psi_x^{(1)} - \left(\psi_y^{(1)}\right)^2 + \bar{\psi}_y^{(1)}\cdot\psi_y^{(1)}\right)\\
c &= -\left(\psi^{(0)}\right)^2 + \left(\psi_x^{(1)}\right)^2 + \left(\psi_y^{(1)}\right)^2.
\end{aligned}$$

Since $r(\theta)$ is a quadratic polynomial, it possibly has two zeros in the set $[0, 1]$. Due to convexity, the largest zero in this set is the correct choice for θ_s, since it corresponds to the intersection with the $\psi^{(0)} \geq 0$ part of the double cone $|\psi^{(1)}|^2 \leq (\psi^{(0)})^2$, while the smaller zero (which is by definition farther away from $\bar{U}_K$) corresponds to the intersection with the $\psi^{(0)} \leq 0$ part of the double cone. Finally, set $\theta := \max_s\theta_s$.

Note that in each intermediate step of the Runge–Kutta scheme the realizability limiter is always applied after the slope limiting. Applying the slope limiter can destroy the realizability again [29].

Table 1
Abbreviation of limiter combinations. Setting $M = \infty$ is equivalent to disabling the slope limiter. □ and △ correspond to the rectangular and triangular meshes, respectively.

Abbr.	Explanation
SLM□/△	Slope limiter in primitive variables with the constant M specified
CLM□/△	Slope limiter in characteristic variables with the constant M specified
SRLM□/△	Slope limiter in primitive variables + realizability limiter
CRLM□/△	Slope limiter in characteristic variables + realizability limiter

5. Numerical results

In this section, we compare the performance of the RKDG schemes on unstructured triangular meshes and uniform rectangular meshes for various combinations of limiters. Specifically we consider the limiter combinations given in Table 1. The time step is taken as indicated by (4.1).

To ensure that our research is reproducible, the codes used in this publication can be found on *GitHub*, see [47].

In the numerical results that follow we denote the mesh size on both unstructured triangular meshes and uniform rectangular meshes by h. All plots show either the zeroth moment $\psi^{(0)}$ or the norm of the first normalized moment $|\phi^{(1)}| = |\frac{\psi^{(1)}}{\psi^{(0)}}|$. The loss of realizability is indicated in the latter by the use of black ($|\phi^{(1)}| > 1$) and white ($\psi^{(0)} < 0$) colors.

Before we describe the test cases and the results, we detail some of the steps in the algorithm, and the computation of the errors.

Fixing a DG solution which is not realizable. In test cases where the realizability limiter is not used (SLM/CLM) the solution may violate the realizability condition and thus the flux function cannot be evaluated. We therefore compute a modified numerical solution which we use only to compute the flux, i.e. the actual solution in each cell remains the same. We modify the values of the numerical solution locally at each Gauss point as follows: let ϵ be a specified numerical tolerance, if $\psi^{(0)} < \epsilon$ then we set $\psi^{(0)} = \epsilon$. In addition, if the normalized first moment

$$f := |\frac{\psi^{(1)}}{\psi^{(0)}}| > (1-\epsilon),$$

we modify the values of first moment as follows: $\psi_x^{(1)} = \frac{\psi_x^1}{f}(1-\epsilon)$ and $\psi_y^{(1)} = \frac{\psi_y^1}{f}(1-\epsilon)$. We choose a tolerance of $\epsilon = 10^{-12}$.

Transformation to characteristic variables.

In the case of the triangular meshes the matrices $\mathcal{R}$ and $\mathcal{R}^{-1}$ from (3.19) are computed using the GSL linear algebra package [48] while they can be precomputed analytically in case of the rectangular grid. The transformation to and from the characteristic variables is achieved by left multiplying the variables by $\mathcal{R}^{-1}$ and $\mathcal{R}$, respectively.

In case that we need the transformation to characteristic variables and do not use the realizability limiter (i.e. CLM), we use the same realizability fix as in the flux function, but for the computation of the transformation matrices only. This ensures that transformation matrices are invertible due to the strict hyperbolicity of the moment system in the interior of the realizable set. The transformation matrix has a condition number of roughly $2/\epsilon$, where ϵ is the distance of the (cell mean of the) normalized first moment to the realizability boundary. Note that this implies that close to the realizability boundary, significant round-off errors may occur. However, we have performed numerical experiments with the linesource test case with $\epsilon = 10^{-5}, 10^{-12}, 10^{-14}$, and observed no significant effect of the cutoff parameter.

Comparison to a reference solution. We note that for a general $f > 0$ we have that

$$\|\log_{10}(f)\|_{H^1(K)} = \|\log_{10}(f)\|_{L^2(K)} + \|\frac{1}{\log_{10} f}\nabla_x f\|_{L^2(K)}.$$

We can therefore use the evaluation of the DG polynomial and its first-order derivatives in every element K to calculate its logarithmic Sobolev representation locally.

The reference solution is computed using a first-order Lax–Friedrichs finite-volume scheme on an equidistant rectangular grid with 8192×8192 grid points. The gradients for the reference solution are obtained using centered finite difference formulas. Finally, the argument in the norm is evaluated on every point of the reference grid and integrated using a quadrature with equal weights at exactly those reference points (rectangle rule).

Choosing the limiter parameter M. The solutions of the benchmark test cases that follow are plotted on a logarithmic scale. We thus choose the value of M in (3.18), using the logarithmic Sobolev norm error, as

$$M = \text{argmin}_{M\geq 0}\|\log_{10}\left(\psi_M^{(0)}\right) - \log_{10}\left(\psi_{ref}^{(0)}\right)\|_{H^1(X)}. \tag{5.1}$$

Since every evaluation of (5.1) requires to solve the full system of equations, finding the true minimum using e.g. a gradient method is not feasible. We therefore restricted ourselves to the discrete set of (almost) logarithmically spaced values $M \in \mathcal{M} := \{0.1, 0.2, 0.5, 1, 2, 10, 22, 46, 100, 150\}$.

Table 2
L^1- and L^∞-errors and observed convergence order ν for the first component of the realizability-limited, piece-wise linear and quadratic reconstructions of $U(x, y)$ from (5.2) with $\xi = 10^{-4}$.

$1/h$	$k=1$					$k=2$				
	E_h^1	ν	E_h^∞	ν	$\theta_{\max}$	E_h^1	ν	E_h^∞	ν	$\theta_{\max}$
5	5.535e−02	–	2.790e−01	–	3.210e−01	1.787e−02	–	6.567e−02	–	1.783e−01
10	1.252e−02	2.1	1.269e−01	1.1	3.960e−01	1.483e−03	3.6	1.153e−02	2.5	5.305e−02
20	2.774e−03	2.2	3.831e−02	1.7	4.117e−01	1.382e−04	3.4	1.495e−03	2.9	1.391e−02
40	6.500e−04	2.1	1.001e−02	1.9	4.154e−01	1.551e−05	3.2	1.878e−04	3.0	3.519e−03
80	1.568e−04	2.1	2.531e−03	2.0	4.164e−01	1.881e−06	3.0	2.350e−05	3.0	8.824e−04
160	3.847e−05	2.0	6.345e−04	2.0	4.166e−01	2.332e−07	3.0	2.938e−06	3.0	2.205e−04
320	9.526e−06	2.0	1.587e−04	2.0	4.166e−01	2.909e−08	3.0	3.673e−07	3.0	5.431e−05

5.1. Failure of the realizability limiter

We want to extend the investigation in [27] to our two-dimensional setup. Define the two moment vectors

$$U_0 = (1-\xi)\begin{pmatrix}1\\1\\0\end{pmatrix} + \xi\begin{pmatrix}1\\0\\0\end{pmatrix}, U_1 = 10^{-6}\cdot\left((1-\xi)\begin{pmatrix}1\\0\\1\end{pmatrix} + \xi\begin{pmatrix}1\\0\\0\end{pmatrix}\right).$$

Both of them satisfy $|\frac{\psi^{(1)}}{\psi^{(0)}}| = 1-\xi$, i.e. the distance to the realizability boundary can be controlled by the parameter ξ. Due to the convexity of the realizable set every convex combination of U_0 and U_1 will be realizable as well. We can thus define the vector of functions

$$\begin{aligned} U(x,y) &= (1-\lambda(x,y))U_0 + \lambda(x,y)U_1, \\ \lambda(x,y) &= \frac{\cos(2(x+y)\pi)+1}{2} \in [0,1], \end{aligned} \tag{5.2}$$

which is realizable for all $(x, y) \in [0, 1]^2$.

Now we discretize the domain, for simplicity, using the structured rectangular mesh with equidistant step sizes. We project $U(x, y)$ onto the DG basis of degree k, $k \in \{0, 1, 2\}$ and apply the realizability-preserving limiter from Section 4. Then we refine the grid and calculate L_1- and L_∞-errors for the zeroth moment $\psi^{(0)}$ as

$$E_h^1 = \int_0^1\int_0^1 \left|\psi_a^{(0)}(x,y) - \psi_h^{(0)}(x,y)\right| dxdy, \quad E_h^\infty = \max_{(x,y)\in[0,1]^2}\left|\psi_a^{(0)}(x,y) - \psi_h^{(0)}(x,y)\right|,$$

where $\psi_a^{(0)}$ denotes the exact zeroth moment of U and $\psi_h^{(0)}$ its limited DG polynomial. In practice, the integral in E_h^1 is approximated by a high-order tensor Gaussian quadrature on every cell and the max in E_h^∞ is taken over the same quadrature nodes.

The observed convergence order ν is defined by

$$\frac{E_{h1}^p}{E_{h2}^p} = \left(\frac{h_1}{h_2}\right)^\nu \tag{5.3}$$

where for $i \in \{1, 2\}$, E_{hi}^p is the error E_h^p for the numerical solution using cell size h_i, for $p \in \{1, \infty\}$.

We found that taking $\xi \in [0, 10^{-4}]$ places the moment curve $U(x, y)$ close enough to the boundary of realizability that the realizability limiter was active for every number of cells we considered. In Table 2 we show convergence rates for $\xi = 10^{-4}$. These results show the expected convergence order $k + 1$ in all cases. In this table we include the column $\theta_{\max}$, which gives the maximum value of θ from the realizability limiter over all spatial cells. That $\theta_{\max}$ is nonzero in each row indicates that the realizability limiter was active for every reconstruction.

Pushing U closer to the realizability boundary ($\xi \leq 10^{-5}$) degrades the convergence order of the piecewise-linear reconstruction, verifying the mentioned convergence problems. This is demonstrated in Table 3 for the extreme case $\xi = 0$, i.e. moments are placed on the realizability boundary. Surprisingly, the third-order approximation has the full convergence order for all tested $\xi \in [0, 10^{-3}]$. Note that this is different to the results in [27] where the third-order approximation degrades to second order. The reason for this is still unclear but might be due to the high non-linearity of the M_3 model used in [27]. We checked several variants of the test (by choosing different vectors on the unit sphere instead of $(1, 0, 0)^T$ and modifying the weight 10^{-6} in front of U_1) and all showed the same behavior.

Full convergence tests for this scheme in one and two dimensions can be found in [27,29].

5.2. Line source

Our first benchmark is the line-source test as proposed in [49]. It is a Green's function problem, where a pulse of particles is emitted from a line in an infinite medium. This corresponds to an initial condition of the form $\psi^{(0)}(x, y) = c \cdot \delta(x, y)$,

Table 3
L^1- and L^∞-errors and observed convergence order ν for the first component of the realizability-limited, piece-wise linear and quadratic reconstructions of $U(x, y)$ from (5.2) with $\xi = 0$.

$1/h$	$k = 1$					$k = 2$				
	E_h^1	ν	E_h^∞	ν	$\theta_{\max}$	E_h^1	ν	E_h^∞	ν	$\theta_{\max}$
5	6.716e−02	–	3.594e−01	–	5.603e−01	1.787e−02	–	6.567e−02	–	1.783e−01
10	1.532e−02	2.1	1.269e−01	1.5	3.960e−01	2.033e−03	3.1	1.153e−02	2.5	5.305e−02
20	3.143e−03	2.3	3.831e−02	1.7	4.117e−01	1.577e−04	3.7	1.495e−03	2.9	1.391e−02
40	6.966e−04	2.2	1.001e−02	1.9	4.154e−01	1.614e−05	3.3	1.878e−04	3.0	3.519e−03
80	1.626e−04	2.1	2.531e−03	2.0	4.164e−01	1.901e−06	3.1	2.350e−05	3.0	8.829e−04
160	3.920e−05	2.1	6.345e−04	2.0	4.166e−01	2.338e−07	3.0	2.938e−06	3.0	2.217e−04
320	9.625e−06	2.0	3.008e−04	1.1	4.167e−01	2.912e−08	3.0	3.673e−07	3.0	8.294e−05

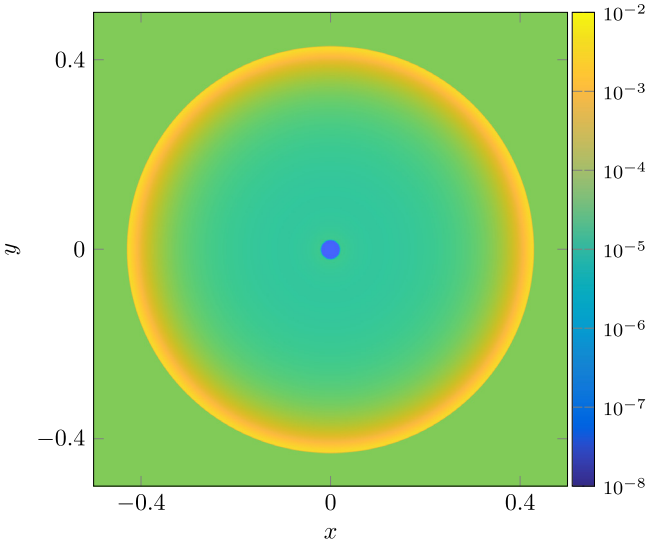

Fig. 3. Line source: $\psi^{(0)}$ of Lax–Friedrichs reference solution on a 8192 × 8192 grid.

whose lack of regularity makes this problem especially hard to tackle for the method of moments, including the M_1 model, see e.g. [50]. The parameters of this test are as follows:

- Domain: $[-0.5, 0.5]^2$ with $h = 0.004$
- Time $T = 0.45$
- Parameters: $\sigma_a = \sigma_s = 0, q^{(0)} = 0, q^{(1)} = 0$
- Initial condition: smoothed Dirac $\psi^{(0)}(x, y) = \max(\exp(-10\frac{x^2+y^2}{\sigma^2}), 10^{-4})$ with $\sigma = 0.02$, $\psi^{(1)}(x, y) = 0$
- Boundary conditions are Dirichlet conditions consistent with the initial conditions. Because the signal does not reach the boundary, these conditions do not influence the result.

Due to the rotational invariance of the initial condition and the flux of the M_1 model the exact solution for the line-source problem has rotational symmetry. (See Fig. 3.)

This symmetry is easily destroyed by the application of the slope limiter in primitive variables (SL0□/△, Fig. 4). It is visible for both mesh types that the solution is strongly asymmetric in density as well as normalized velocity. Furthermore, realizability is lost in parts of the domain (black and white spots).

Applying the characteristic limiter (CL0□/△) yields much better results: the solution is much more symmetric and as shown in Tables 4 and 5, it is even realizable in the mean at the final time step. However, the realizability in the mean does not hold at every time step and in addition there are a Gauss points on both meshes at which the solution is unrealizable. We note that the fact that primitive-variable limiting (SL0□/△) can result in non-physical oscillations is a well-known phenomenon and has been reported in case of the M_1 model in one dimension in [13].

Unfortunately, choosing $M = 0$ in the minmod limiter results in a flattening of the solution at smooth extrema and first-order convergence in the L_∞-norm [16]. Setting $M = 22$ results in sharper solutions in the sense that the width of the wave front is decreasing (Fig. 5). However, this comes at the price of a realizability loss resulting in a complete destruction of the solution (see e.g. CL22□ in Fig. 5). Similar results occur with the primitive-variable limiter (not shown). This can be fixed by further application of the realizability limiter (CRL22□/△). The now-realizable solutions show the same sharpness as with CL22□/△. Furthermore, good rotational symmetry is still visible.

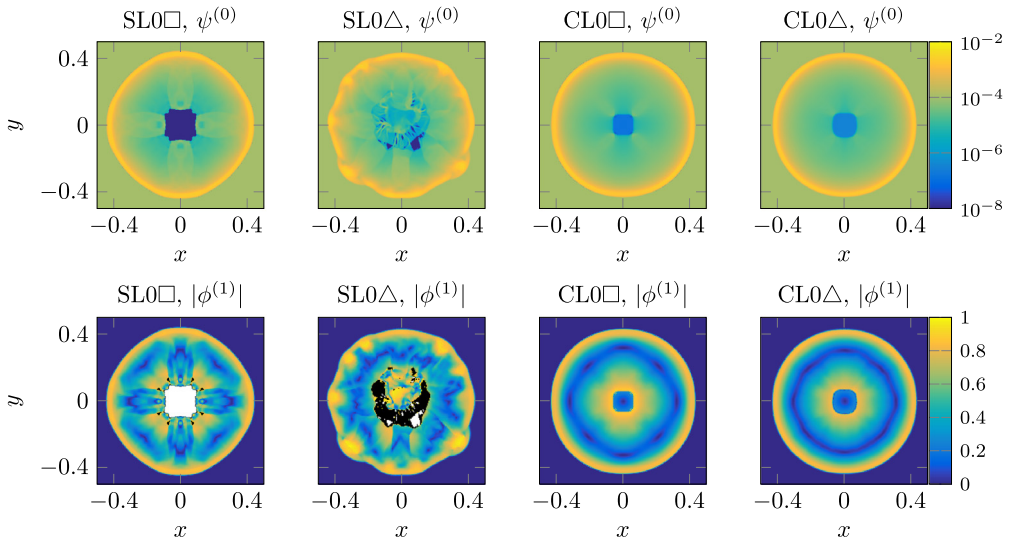

Fig. 4. Line source: comparison of primitive and characteristic slope limiter.

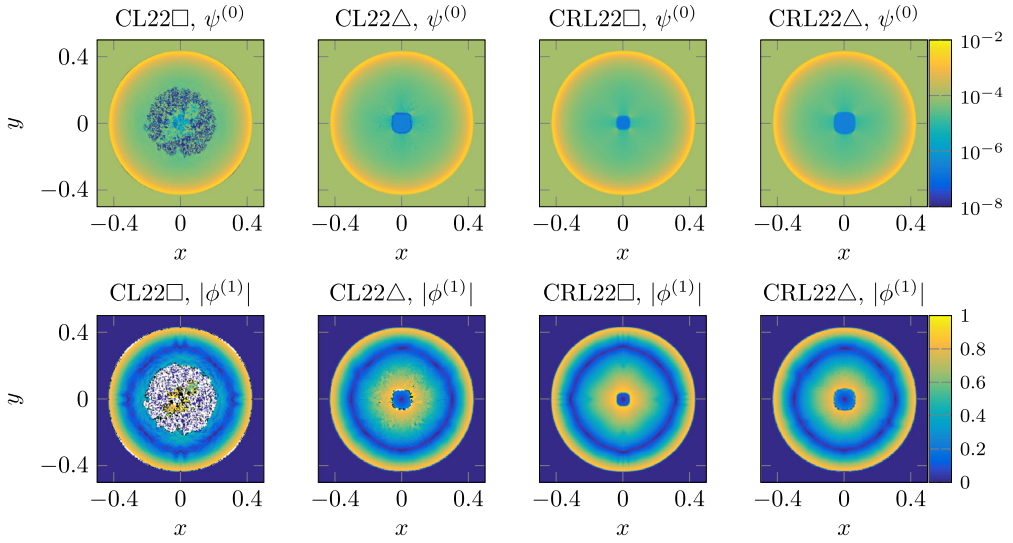

Fig. 5. Line source: comparison of the characteristic limiter with and without realizability limiter.

Table 4
Line source: percentage of non-realizable cells and quadrature points on rectangular mesh.

	SL∞□	SL0□	SL22□	CL0□	CL22□
$\max_t$ GP	11.49%	8.19%	13.01%	0.84%	7.69%
$\max_t$ CM	10.09%	8.08%	10.59%	0.81%	5.87%
GP(t_f)	11.49%	3.26%	13.01%	0.06%	7.69%
CM(t_f)	10.09%	3.15%	10.59%	0.00%	5.87%

A natural question arising is if the realizability limiter on its own is enough to provide a good solution. It has been shown in [13] that even in one dimension spurious oscillations can occur. Similarly, as shown in Fig. 6, symmetry is not preserved and slight oscillations are visible, especially in the normalized velocity. Although the solution is everywhere realizable, a slope limiter is strictly necessary to dampen the Gibbs phenomenon. Similar observations have been made in case of the Euler equations in [44,51].

Table 5
Line source: percentage of non-realizable cells and quadrature points on triangular mesh.

	SL∞△	SL0△	SL22△	CL0△	CL22△
$\max_t$ GP	81.01%	5.01%	30.10%	0.03%	0.33%
$\max_t$ CM	80.33%	5.03%	25.12%	0.00%	0.17%
GP(t_f)	81.01%	5.05%	30.10%	0.01%	0.20%
CM(t_f)	80.33%	5.00%	25.12%	0.00%	0.08%

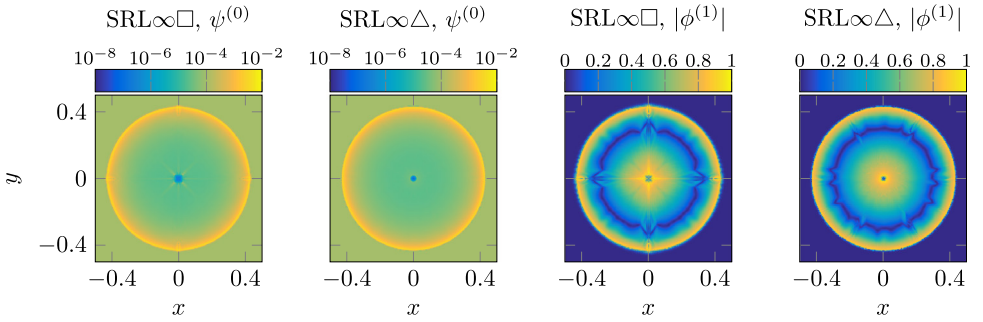

Fig. 6. Line source: realizability limiter only.

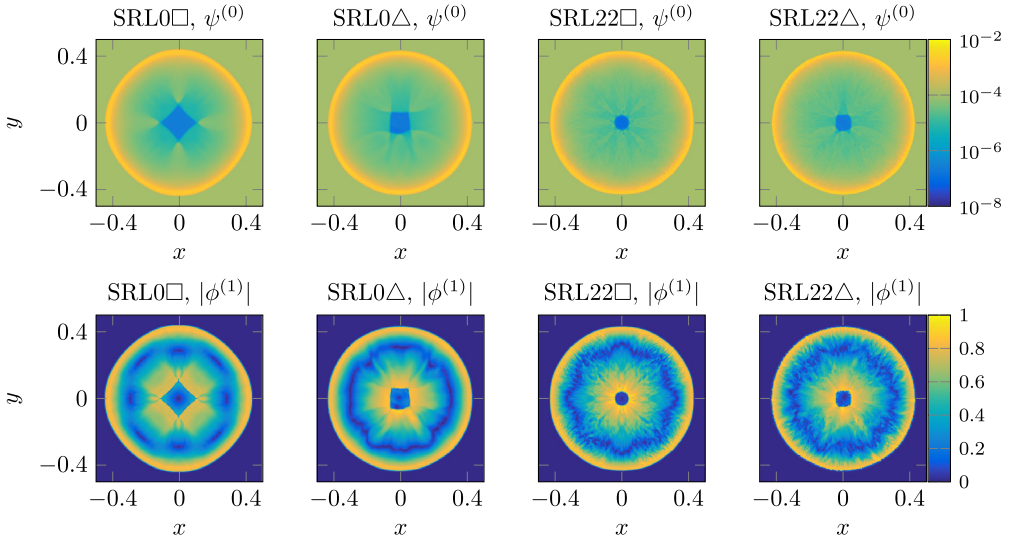

Fig. 7. Line source: primitive variable and realizability limiter.

As we have shown, using the characteristic and realizability limiter together yields good results. However, the change to characteristic fields is expensive and the transformation matrices become arbitrarily poorly conditioned close to the realizability boundary [52], yielding inaccurate results. Unfortunately, Fig. 7 shows that the combination of limiting in the primitive-variable and realizability limiter is not enough to obtain good results. It appears that these solutions are even worse than the realizability-limiter-only solutions shown in Fig. 6.

Our numerical tests show that in general the characteristic limiter combined with the realizability limiter (CRLM) is superior to the combination of limiting in the components and the realizability limiter (SRLM). However, the differences between the two limiting strategies are most dramatic for the linesource test case. In the rest of the problems we consider, the solutions both look good and are comparable.

In Tables 4 and 5 we summarize the performance of the slope limiter in the absence of the realizability limiter by counting the proportion of non-realizable cells (CM) and Gauss points (GP). We provide both the maximum values in the time interval (taken over a sample of 20 equidistant time points) and the values at the final time step for each mesh. It is clear that the characteristic limiter (CL*M*□/△) performs better than the slope limiter in primitive variables (SL*M*□/△). In fact the final solution from the characteristic limiter (CL0□/△) is realizable in the mean on both meshes. However, realizability in the

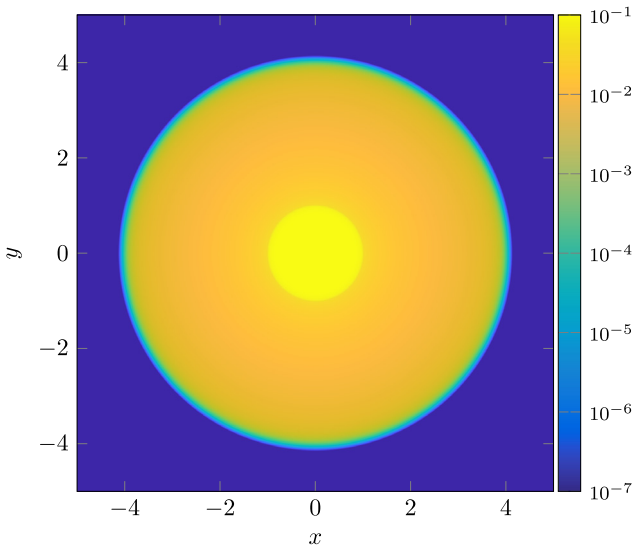

Fig. 8. Homogeneous disk: $\psi^{(0)}$ of Lax–Friedrichs reference solution on a 8192 × 8192 grid.

Table 6
Homogeneous disk: percentage of non-realizable cells and quadrature points on rectangular mesh.

	SL∞□	SL0□	SL0.2□	CL0□	CL0.2□
$\max_t$ GP	24.13%	12.46%	18.95%	1.57%	5.53%
$\max_t$ CM	21.95%	7.19%	15.08%	0.22%	1.14%
GP(t_f)	4.93%	12.46%	18.46%	1.23%	2.91%
CM(t_f)	0.26%	7.19%	9.39%	0.06%	0.06%

mean and at the Gauss points is not guaranteed at all time steps on the time interval. These results further reinforce the need for the realizability limiter.

5.3. Homogeneous disk

Our next test case is the two-dimensional version of the homogeneous sphere test, which is often used to test radiation transport codes, see e.g. [53–56]. It consists of a static homogeneous and isothermal sphere that radiates in vacuum [57]. It is well-suited to test moment approximations since it admits an analytical stationary solution for the underlying kinetic transport equation [58]. The parameters in the two-dimensional setting are as follows:

- Domain: $[-5, 5]^2$ with $h = 0.05$
- Time: 3.00
- Parameters: Let D be the unit disk $D = \{(x, y) : x^2 + y^2 \leq 1\}$. Set $\sigma_s = 0$; $\sigma_a = 10$ on D, zero otherwise; source $q^{(0)} = 1$ on D, zero otherwise; $q^{(1)} = 0$
- Initial condition: $\psi^{(0)} = 10^{-10}$, $\psi^{(1)} = 0$
- Boundary conditions: $\psi^{(0)} = 10^{-10}$, $\psi^{(1)} = 0$

This test case is numerically challenging due to the discontinuous parameters. Furthermore, its solution is again radially symmetric, simplifying the analysis of the quality of the limiter configurations. (See Fig. 8.)

As in the line source test case, we observe that the application of the primitive-variable limiter results in an oscillatory solution which is not realizable. This is shown in Fig. 9. In case of the triangular mesh strong filaments form at the edge of the disk. Using the characteristic limiter slightly improves the solution. However, and in contrast to the line source, even with $M = 0$ the characteristic limiter is no longer able to preserve realizability in the mean (see Tables 6 and 7), furthermore, a larger proportion of the Gauss points are not realizable. Additionally, at the boundary of the disk the quality of the solution is strongly reduced due to the bad condition number of the transformation matrix, which goes to infinity for values of $|\phi^1|$ approaching 1 [52]. (See Fig. 10.)

Adding the realizability limiter strongly improves the quality of the solution (Fig. 10). As before, choosing $M = 0.2$ gives less diffusive results.

A quantitative analysis of the slope limiters (SLM□/△) and (CLM□/△) show that limiting in characteristic variables yields better results but the solution remains unrealizable.

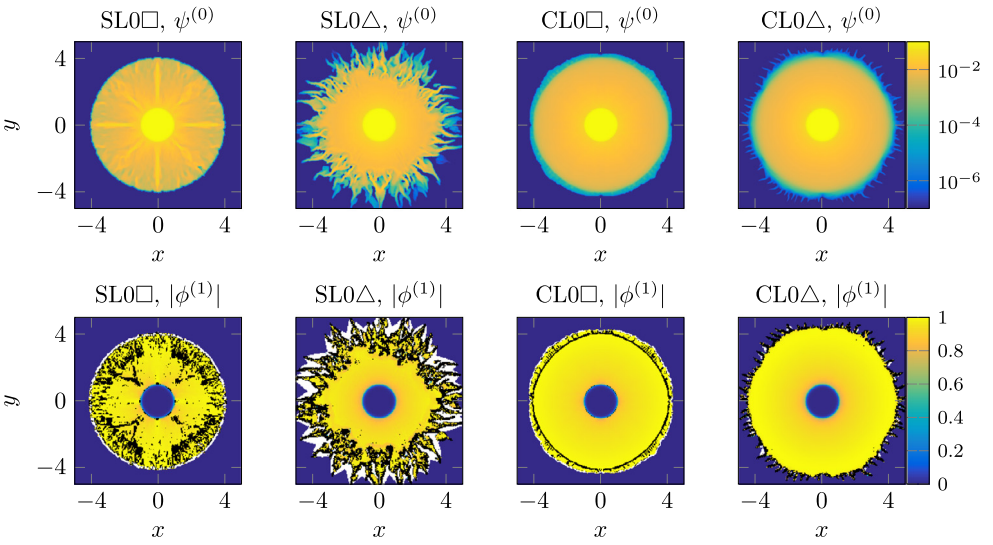

Fig. 9. Homogeneous disk: comparison of primitive and characteristic slope limiter.

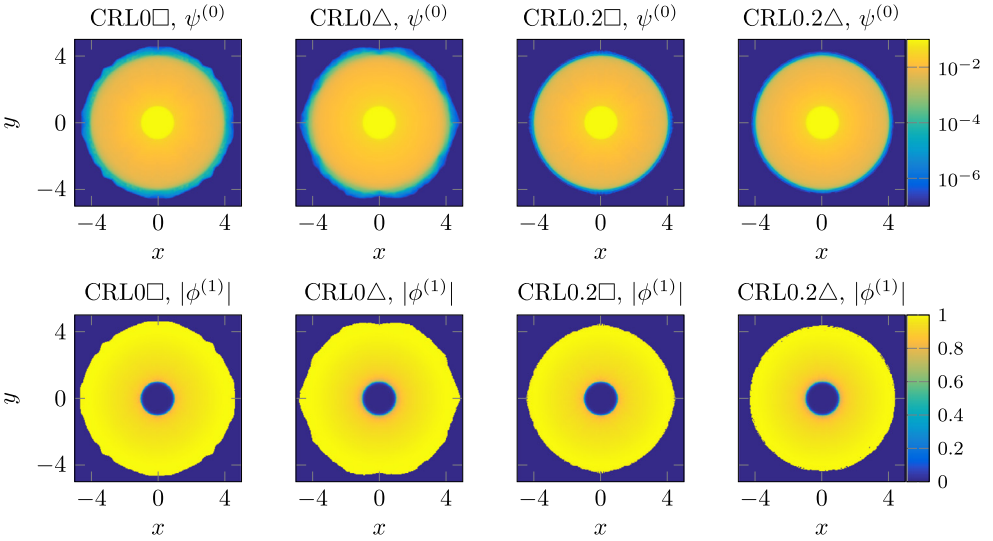

Fig. 10. Homogeneous disk: comparison of the characteristic limiter with and without realizability limiter.

Table 7
Homogeneous disk: percentage of non-realizable cells and quadrature points on triangular mesh.

	SL∞△	SL0△	SL0.2△	CL0△	CL0.2△
$\max_t$ GP	71.75%	34.25%	41.73%	5.65%	33.65%
$\max_t$ CM	71.62%	34.41%	40.18%	5.75%	32.64%
GP(t_f)	71.75%	34.25%	41.73%	5.65%	33.65%
CM(t_f)	71.61%	34.41%	40.18%	5.71%	32.64%

5.4. Flash

In this test case a bulk of mass is moving from the center of the domain to the right boundary [59]. The parameters are given as follows:

- Domain: $[-10, 10]^2$ with $h = 0.06$
- Time: 6

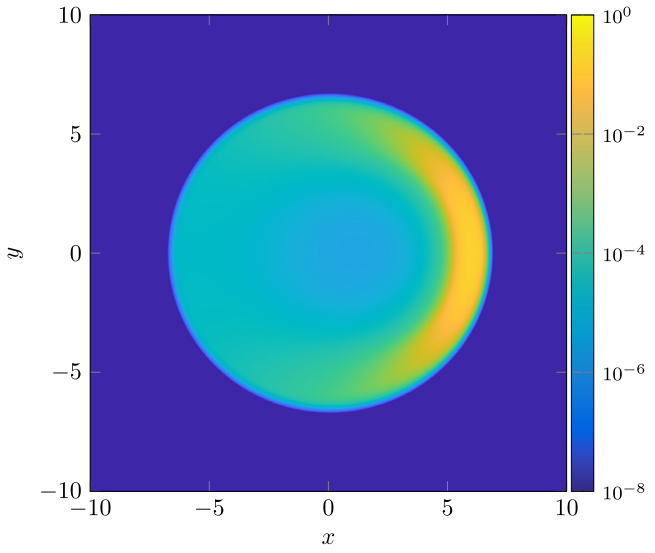

Fig. 11. Flash test: $\psi^{(0)}$ of Lax–Friedrichs reference solution on a 8192 × 8192 grid.

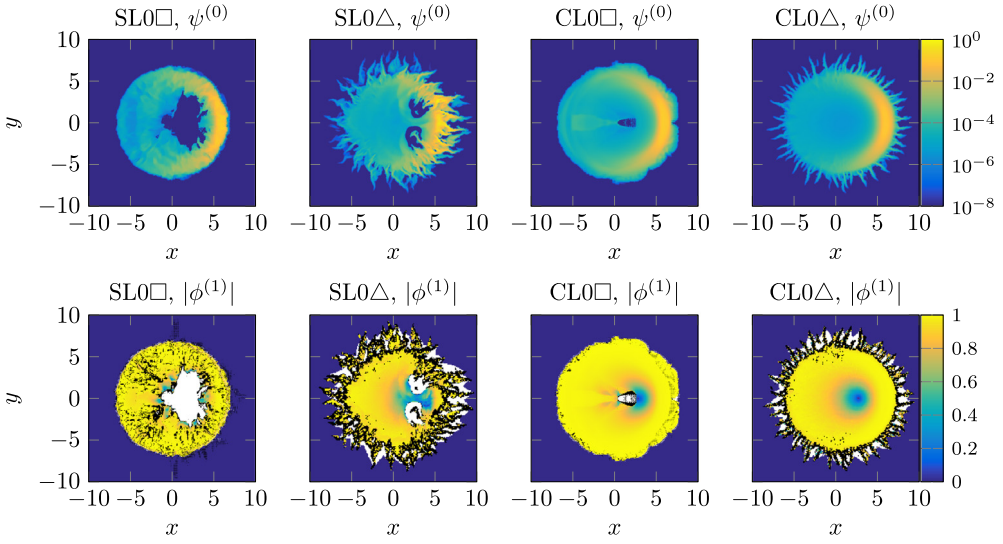

Fig. 12. Flash test: comparison of primitive and characteristic slope limiter.

- Parameters: Let D be unit disk with radius 0.5, $D = \{(x, y) : x^2 + y^2 \leq 0.25\}$. Set $\sigma_s = 0$; $\sigma_a = 0$; source $q^{(0)} = 0$, $q^{(1)} = 0$
- Initial condition: $\psi^{(0)} = 1$, $\psi_x^{(1)} = 0.9$, $\psi_y^{(1)} = 0$ on D, $\psi^{(0)} = 10^{-10}$, $\psi^{(1)} = 0$ otherwise
- Boundary conditions: $\psi^{(0)} = 10^{-10}$, $\psi^{(1)} = 0$

The reference solution at the final time is depicted in Fig. 11.

Due to the initial condition which is placed close to the boundary of realizability this test is well suited to show the inability of standard slope limiters to preserve realizability. This is demonstrated in Fig. 12 where similar effects as before occur.

A comparison of Figs. 12 and 13 confirms that the combination of the characteristic limiter with the realizability limiter yields the best solutions. The performance of the slope limiter without the realizability limiter in Tables 8 and 9 is consistent with previous observations in the line source and homogeneous disk test cases.

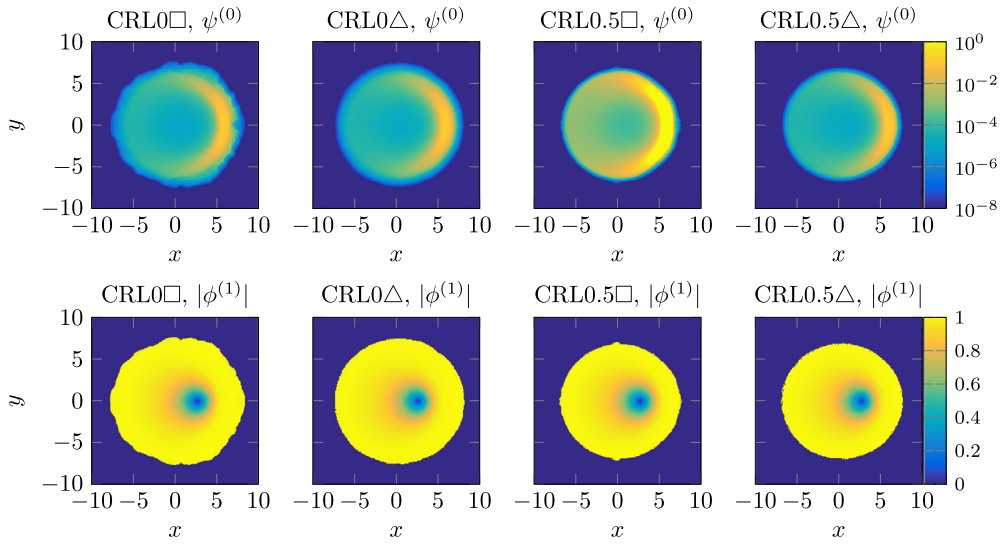

Fig. 13. Flash test: characteristic limiter with realizability limiter for different values of M.

Table 8
Flash: percentage of non-realizable cells and quadrature points on rectangular mesh.

	SL∞□	SL0□	SL0.5□	CL0□	CL0.5□
$\max_t$ GP	14.84%	13.97%	20.88%	0.86%	19.75%
$\max_t$ CM	11.77%	11.53%	14.27%	0.22%	15.01%
GP(t_f)	14.70%	13.97%	20.88%	0.86%	19.75%
CM(t_f)	9.50%	11.53%	14.27%	0.22%	15.01%

Table 9
Flash: percentage of non-realizable cells and quadrature points on triangular mesh.

	SL∞△	SL0△	SL0.5△	CL0△	CL0.5△
$\max_t$ GP	55.21%	24.12%	50.14%	5.45%	50.99%
$\max_t$ CM	55.18%	24.27%	49.10%	5.63%	39.00%
GP(t_f)	55.28%	24.12%	50.14%	5.45%	40.99%
CM(t_f)	55.18%	24.27%	49.10%	5.63%	39.00%

6. Conclusions and outlook

In this work, we have investigated a third order realizability-preserving DG method to approximate solutions to the M_1 model of radiation transport. The results show that in all test cases presented, the realizability limiter is imperative to ensure the realizability of the numerical solutions.

Based on these results, we advocate the M_1 model as an ideal test case that pushes the boundaries of high-order realizability-preserving numerical methods. The model equations are highly nonlinear, and are well-posed only in a geometrically complex (yet convex) domain of realizability. Furthermore, practically relevant solutions are not just wave fronts, but rather beam-like solutions, or they possess Dirac-like source terms. Solutions and material coefficients tend to vary over several orders of magnitude. Furthermore, so-called source-detector problems in radiation transport require an accurate solution (in terms of the relative error) at one or more specific points in space.

The results presented in this paper cast some doubt on whether DG is a competitive numerical scheme for M_1, considering the accuracy requirements commonly encountered in practice. For instance, for the homogeneous disk test case the DG solution possesses around 10^6 degrees of freedom. It is comparable in quality to a Lax–Friedrichs (LF) solution with roughly the same number of degrees of freedom ($2048 \times 2048 \approx 4 \cdot 10^6$), which however is significantly faster to compute because no limiting is needed. Similarly, in the line source test case, the best DG solution is comparable to a 1024×1024 LF solution.

In several test cases, the high-order DG method yields reliable results only if a full limiting strategy is employed, including transformations to and from the characteristic variables. Not only do those transformations incur a significant cost, they also become less and less well conditioned when higher accuracy requirements are imposed. It is therefore questionable whether, for the M_1 model, the high-order DG methodology will ever become more efficient than a simple monotone first-order scheme that automatically guarantees realizability.

That being said, it should be pointed out that the DG methodology studied here, albeit being an established standard method, can most certainly be improved. For instance, more sophisticated limiting techniques, such as WENO limiting with KXRCF shock detection [60,61], or limiters that incorporate high-order approximations during the limiting process [62,63], could be combined with the realizability-preserving limiter. This would remove the need for the problem-dependent minmod parameter M. Furthermore, more efficient time stepping schemes could be applied, such as explicit low-storage SSP Runge–Kutta schemes [64], SSP multi-step Runge–Kutta methods [65,66] (which both require less evaluations of the differential operator $\mathcal{L}_h$), or even Implicit–Explicit schemes [67,68] (to remove the dependence on the right-hand side (σ_a and σ_s) in the CFL condition (4.1)).

Further research steps include realizability limiting for higher-order minimum-entropy models (i.e., M_N with $N \geq 2$) in two and three dimensions, similar to [27]. The main challenge in that context is that a complete characterization of the realizability set by means of simple algebraic criteria is still outstanding. One possible remedy is to use discrete realizability criteria with respect to a quadrature rule [52]. Moreover, in general a high number of quadrature points is necessary to produce solutions without discernible discrete ray artifacts [27,29,50], resulting in an extremely high cost for realizability limiting. Hence less expensive strategies to guarantee realizability need to be developed.

Acknowledgments

B. Seibold wishes to acknowledge support by the National Science Foundation, United States under grant DMS-1719640. M. Frank acknowledges support from Deutsche Forschungsgemeinschaft (DFG), Germany under Grant FR 2841/6-1. We thank Philipp Monreal for co-developing the unstructured-mesh DG code.

Appendix A. Supplementary data

Supplementary material related to this article can be found online at https://doi.org/10.1016/j.cam.2018.04.017.

References

[1] C.D. Levermore, Relating Eddington factors to flux limiters, J. Quant. Spectrosc. Radiat. Transfer 31 (1984) 149–160.
[2] T.A. Brunner, J.P. Holloway, One-dimensional Riemann solvers and the maximum entropy closure, J. Quant. Spectrosc. Radiat. Transfer 69 (2001) 543–566.
[3] E. Toro, Riemann Solvers and Numerical Methods for Fluid Dynamics: A Practical Introduction, Springer, ISBN: 9783540252023, 2009.
[4] W. Dreyer, Maximisation of the entropy in non-equilibrium, J. Phys. A 20 (1987) 6505–6517.
[5] B. Dubroca, J.L. Feugeas, Entropic hierarchy for the radiative transfer equation, C. R. Acad. Sci. Paris Ser. I 329 (1999) 915–920.
[6] M. Frank, H. Hensel, A. Klar, A fast and accurate moment method for the Fokker–Planck equation and applications to electron radiotherapy, SIAM. J. Appl. Math. 67 (2) (2007) 582–603.
[7] E.T. Jaynes, Information theory and statistical mechanics, Phys. Rev. 106 (4) (1957) 620.
[8] C.D. Levermore, Moment closure hierarchies for kinetic theories, J. Stat. Phys. 83 (5–6) (1996) 1021–1065.
[9] I. Müller, T. Ruggeri, Rational Extended Thermodynamics, second ed., Springer-Verlag, New York, 1993.
[10] A. Ore, Entropy of radiation, Phys. Rev. 98 (1955) 887.
[11] P. Rosen, Entropy of radiation, Phys. Rev. 96 (1954) 555.
[12] R. LeVeque, Finite volume methods for hyperbolic problems, 2002.
[13] E. Olbrant, C.D. Hauck, M. Frank, A realizability-preserving discontinuous Galerkin method for the M_1 model of radiative transfer, J. Comput. Phys. 231 (17) (2012) 5612–5639.
[14] W. Reed, T. Hill, Triangular mesh methods for neutron transport equation, Los Alamos Scientific Laboratory Report, LA-UR-73-479, 1973.
[15] B. Cockburn, S. Hou, C.-W. Shu, TVB Runge-Kutta local projection discontinuous Galerkin finite element method for conservation laws IV: The multi-dimensional case, Math. Comp. 54 (1990) 545–581.
[16] B. Cockburn, C.-W. Shu, TVB Runge-Kutta local projection discontinuous Galerkin finite element method for conservation laws II: General framework, Math. Comp. 52 (186) (1989) 411–435.
[17] B. Cockburn, C.W. Shu, The Runge-Kutta local projection P^1-discontinuous-Galerkin finite element method for scalar conservation laws, ESAIM Math. Model. Numer. 25 (3) (1991) 337–361.
[18] B. Cockburn, S.-Y. Lin, C.-W. Shu, TVB Runge-Kutta local projection discontinuous Galerkin finite element method for consevation laws III: One-dimensional systems, J. Comput. Phys. 84 (1989) 90–113.
[19] B. Cockburn, C.-W. Shu, The Runge–Kutta Discontinuous Galerkin Method for Conservation Laws V: Multidimensional Systems, J. Comput. Phys. 141 (2) (1998) 199–224.
[20] C.-W. Shu, Essentially non-oscillatory and weighted essentially non-oscillatory schemes for hyperbolic conservation laws, 1998, http://link.springer.com/chapter/10.1007/BFb0096355.
[21] R. Biswas, K.D. Devine, J.E. Flaherty, Parallel, adaptive finite element methods for conservation laws, Appl. Numer. Math. 14 (1) (1994) 255–283.
[22] B. Cockburn, C.-W. Shu, Runge–Kutta discontinuous Galerkin methods for convection-dominated problems, J. Sci. Comput. 16 (3) (2001) 173–261.
[23] F. Li, L. Xu, S. Yakovlev, Central discontinuous Galerkin methods for ideal MHD equations with the exactly divergence-free magnetic field, J. Comput. Phys. 230 (12) (2011) 4828–4847.
[24] H. Liu, K. Xu, A Runge-Kutta discontinuous Galerkin method for viscous flow equations, J. Comput. Phys. 224 (2) (2007) 1223–1242.
[25] C. Liang, F. Ham, E. Johnsen, Discontinuous Galerkin Method with WENO Limiter for Flows with Discontinuity, Technical Report, Center for Turbulence Research, 2009.
[26] H. Liu, K. Xu, A gas-kinetic discontinuous Galerkin method for viscous flow equations, J. Mech. Sci. Technol. 21 (9) (2007) 1344–1351.
[27] G.W. Alldredge, F. Schneider, A realizability-preserving discontinuous Galerkin scheme for entropy-based moment closures for linear kinetic equations in one space dimension, J. Comput. Phys. 295 (2015) 665–684.
[28] D. Kershaw, Flux Limiting Nature's Own Way: A New Method for Numerical Solution of the Transport Equation, Technical Report, LLNL Report UCRL-78378, 1976.

[29] F. Schneider, Moment Models in Radiation Transport Equations, Dr. Hut Verlag, 2016, p. 260.
[30] P. Monreal, Moment Realizability and Kershaw Closures in Radiative Transfer (Ph.D. thesis), TU Aachen, 2012.
[31] J.-F. Coulombel, F. Golse, T. Goudon, Diffusion approximation and entropy-based moment closure for kinetic equations, Asymptotic. Anal. 45 (1,2) (2005) 1–39.
[32] C. Berthon, P. Charrier, B. Dubroca, An HLLC scheme to solve the M_1 model of radiative transfer in two space dimensions, J. Sci. Comput. 31 (3) (2006) 347–389.
[33] S. Gottlieb, C.-W. Shu, E. Tadmor, Strong stability-preserving high-order time discretization methods, SIAM Rev. 43 (1) (2001) 89–112.
[34] G.C. Pomraning, Variational boundary conditions for the spherical harmonics approximation to the neutron transport equation, Ann. Physics 27 (2) (1964) 193–215.
[35] E.W. Larsen, G.C. Pomraning, The PN Theory as an asymptotic limit of transport theory in planar geometry I: analysis, Nucl. Sci. Eng. 109 (1) (1991) 49–75.
[36] R.P. Rulko, E.W. Larsen, G.C. Pomraning, The PN theory as an asymptotic limit of transport theory in planar geometry II: Numerical results, Nucl. Sci. Eng. 109 (1) (1991) 76–85.
[37] H. Struchtrup, Kinetic schemes and boundary conditions for moment equations, Z. Angew. Math. Phys. (ISSN: 00442275) 51 (3) (2000). http://dx.doi.org/10.1007/s000330050002.
[38] C.D. Levermore, Boundary Conditions for Moment Closures, Institute for Pure and Applied Mathematics University of California, Los Angeles, CA on May, 2009.
[39] C. Shu, TVD time discretizations, SIAM J. Sci. Stat. Comput. 9 (1988) 1073–1084.
[40] C.-W. Shu, S. Osher, Efficient implementation of essentially non-oscillatory shock-capturing schemes, J. Comput. Phys. 77 (2) (1988) 439–471.
[41] X. Zhang, Y. Xia, C.-W. Shu, Maximum-principle-satisfying and positivity-preserving high order discontinuous Galerkin schemes for conservation laws on triangular meshes, J. Sci. Comput. 50 (1) (2012) 29–62.
[42] B. Cockburn, An introduction to the discontinuous Galerkin method for convection-dominated problems, Advanced Numerical Approximation of Nonlinear ….
[43] J.S. Hesthaven, T. Warburton, Nodal Discontinuous Galerkin Methods: Algorithms, Analysis, and Applications, Springer Science & Business Media, 2007.
[44] X. Zhang, C.W. Shu, On positivity-preserving high order discontinuous Galerkin schemes for compressible Euler equations on rectangular meshes, J. Comput. Phys. 229 (23) (2010) 8918–8934.
[45] Y. Xing, X. Zhang, Positivity-preserving well-balanced discontinuous Galerkin methods for the shallow water equations on unstructured triangular meshes, J. Sci. Comput. (2013) 1–35.
[46] X. Zhang, C.-W. Shu, A minimum entropy principle of high order schemes for gas dynamics equations, Numer. Math. 121 (3) (2012) 545–563.
[47] P. Chidyagwai, F. Schneider, P. Monreal, Realizability-preserving Runge-Kutta Discontinuous-Galerkin schemes for the M1 model of radiative transfer: Code, 2016.
[48] B. Gough, GNU Scientific Library Reference Manual, third ed., Network Theory Ltd., 2009, ISBN: 0954612078, 9780954612078.
[49] T.A. Brunner, J.P. Holloway, Two-dimensional time dependent Riemann solvers for neutron transport, J. Comput. Phys. 210 (September 2001) (2005) 386–399.
[50] C.K. Garrett, C.D. Hauck, A Comparison of moment closures for linear kinetic transport equations: The line source benchmark, Transp. Theory. Stat. Phys. (2013).
[51] C. Wang, X. Zhang, C.W. Shu, J. Ning, Robust high order discontinuous Galerkin schemes for two-dimensional gaseous detonations, J. Comput. Phys. 231 (2) (2012) 653–665.
[52] G. Alldredge, C. Hauck, A. Tits, High-order entropy-based closures for linear transport in slab geometry II: A computational study of the optimization problem, SIAM. J. Sci. Comput. 34 (4) (2012) B361–B391.
[53] E. Abdikamalov, A. Burrows, C.D. Ott, F. Löffler, E. O'Connor, J.C. Dolence, E. Schnetter, A New Monte Carlo method for time-dependent neutrino radiation transport, Astrophys. J. 755 (2) (2012) 111.
[54] S.W. Bruenn, Stellar core collapse - Numerical model and infall epoch, Astrophys. J. Suppl. Ser. 58 (1985) 771.
[55] M. Rampp, H.T. Janka, Radiation hydrodynamics with neutrinos: Variable Eddington factor method for core-collapse supernova simulations, Astron. Astrophys. 396 (2002) 42.
[56] K. Sumiyoshi, S. Yamada, Neutrino transfer in three dimensions for core-collapse supernovae. I. Static configurations, Astrophys. J. Suppl. Ser. 199 (1) (2012) 17.
[57] D. Radice, E. Abdikamalov, L. Rezzolla, C.D. Ott, A new spherical harmonics scheme for multi-dimensional radiation transport I. Static matter configurations, J. Comput. Phys. 242 (2013) 648–669.
[58] J.M. Smit, J. Cernohorsky, C.P. Dullemond, Hyperbolicity and critical points in two-moment approximate radiative transfer, Astron. Astrophys. 325 (1997) 203–211.
[59] F. Science, Y. Kanno, T. Harada, T. Hanawa, Kinetic Scheme for Solving the M1 Model of Radiative Transfer, Publ. Astron. Soc. Japan 65 (2007) (2013) 72.
[60] L. Krivodonova, J. Xin, J.-F. Remacle, N. Chevaugeon, J. Flaherty, Shock detection and limiting with discontinuous Galerkin methods for hyperbolic conservation laws, Appl. Numer. Math. 48 (3–4) (2004) 323–338.
[61] J. Qiu, C. Shu, A comparison of troubled cell indicators for Runge-Kutta discontinuous Galerkin methods using WENO Limiters, SIAM J. Sci. Comput. 27 (2005) 995–1013.
[62] A. Burbeau, P. Sagaut, C.-H. Bruneau, A problem-independent limiter for high-order RungeKutta discontinuous galerkin methods, J. Comput. Phys. (ISSN: 0021-9991) 169 (1) (2001) 111–150.
[63] L. Krivodonova, Limiters for high-order discontinuous Galerkin methods, J. Comput. Phys. (ISSN: 0021-9991) 226 (1) (2007) 879–896.
[64] D.I. Ketcheson, Highly efficient strong stability-preserving rungekutta methods with low-storage implementations, SIAM J. Sci. Comput. (ISSN: 1064-8275) 30 (4) (2008) 2113–2136.
[65] D.I. Ketcheson, S. Gottlieb, C.B. Macdonald, Strong stability preserving two-step Runge-Kutta methods, SIAM J. Numer. (2011) 1–24.
[66] C. Bresten, S. Gottlieb, Z. Grant, Strong Stability Preserving Multistep Runge–Kutta Methods. arXiv preprint, 2013.
[67] U. Ascher, S. Ruuth, R. Spiteri, Implicit–explicit Runge-Kutta methods for time-dependent partial differential equations, Appl. Numer. Math. (1997).
[68] A. Kanevsky, M.H. Carpenter, D. Gottlieb, J.S. Hesthaven, Application of implicitexplicit high order RungeKutta methods to discontinuous-Galerkin schemes, J. Comput. Phys. (ISSN: 00219991) 225 (2) (2007) 1753–1781.